Giant bipolar unidirectional photomagnetoresistance

Yucheng Jiang[a,1,2], Anpeng He[a,2], Kai Luo[b,2], Jinlei Zhang[a,2], Guozhen Liu[a], Run Zhao[a], Qing Zhang[c], Zhuo Wang[d], Chen Zhao[c], Lin Wang[e], Yaping Qi[f], Ju Gao[g], Kian Ping Loh[h,i], Andrew T. S. Wee[i,j], and Cheng-Wei Qiu[c,1]

Positive magnetoresistance (PMR) and negative magnetoresistance (NMR) describe two opposite responses of resistance induced by a magnetic field. Materials with giant PMR are usually distinct from those with giant NMR due to different physical natures. Here, we report the unusual photomagnetoresistance in the van der Waals heterojunctions of WSe$_2$/quasi-two-dimensional electron gas, showing the coexistence of giant PMR and giant NMR. The PMR and NMR reach 1,007.5% at −9 T and −93.5% at 2.2 T in a single device, respectively. The magnetoresistance spans over two orders of magnitude on inversion of field direction, implying a giant unidirectional magnetoresistance (UMR). By adjusting the thickness of the WSe$_2$ layer, we achieve the maxima of PMR and NMR, which are 4,900,000% and −99.8%, respectively. The unique magnetooptical transport shows the unity of giant UMR, PMR, and NMR, referred to as giant bipolar unidirectional photomagnetoresistance. These features originate from strong out-of-plane spin splitting, magnetic field–enhanced recombination of photocarriers, and the Zeeman effect through our experimental and theoretical investigations. This work offers directions for high-performance light-tunable spintronic devices.NMR)

photomagnetoresistance | van der Waals heterojunction | WSe$_2$ | two-dimensional electron gas | spin polarization

Ordinary magnetoresistance (MR) is commonly found in conductive materials (1). Most materials show the positive magnetoresistance (PMR) effect originating from the Lorentz force (2, 3), which describes a magnetic field–induced increase of resistance. In contrast, the negative magnetoresistance (NMR) usually results from the spin-dependent scattering in the magnetic materials (4, 5). Large MR effects have attracted much interest for their valuable applications as spintronic sensors and memory devices (6–8). Large PMR or NMR is often governed by a specific physical mechanism, and its rarity motivates many efforts on material selection and structural designment (9–12). Giant MR and colossal MR are two well-known NMR effects and are explained by the Valet–Fert model and Mn^{3+}-O-Mn^{4+} double-exchange mechanism, respectively (13–15). Subsequently, various physical processes have been discovered to achieve significant MRs, including tunneling MR (16–19), the Zeeman effect (20, 21), perfect n–p compensation (22, 23), etc. The invention of a larger MR device is always a topical field fueled by improvements in both theory and device applications.

Distinct in their physical mechanisms, PMR and NMR effects often counteract each other, inevitably rendering one dominant over the other in a single large-MR material. For example, some Weyl semimetals tend to show very large PMR but small NMR (24–26). To the best of our knowledge, there has been no report of the systems with both giant PMR and giant NMR. Through a comprehensive investigation of known materials, we postulate that a conventional single material cannot achieve such a unique magnetic transport; thus, we turn our attention to composite materials. Recent advances in van der Waals (vdW) heterojunctions have led to the development of new high-performance functional devices (27–32). Numerous remarkable properties were found by optimizing the design of atomically thin devices, such as magnetotransport (33), electric gating (34), photoconductivity (35, 36), electroluminescence (37), and so on. Such vdW heterojunctions combine the advantages of multiple materials, which offers a possibility to realize the two competing effects, PMR and NMR, in a single device.

In this work, we fabricated lateral vdW heterojunctions between WSe$_2$ and quasi-two-dimensional electron gas (Q2DEG; WSe$_2$/Q2DEG) on SrTiO$_3$ (STO) substrates (38). Since the vdW heterojunctions are electrically insulating at low temperatures, we focus on the magnetic transport behavior of photocarriers: that is, photomagnetoresistance. In this system, we observe the giant bipolar unidirectional photomagnetoresistance (GBU-PhMR). With the definition of MR = [$R(B)/R(0)$ − 1] × 100%, the single device shows PMR of 1,007.5% at −9 T and NMR of −93.5% at 2.2 T, indicating the coexistence of giant PMR and giant NMR. The MR changes over two orders of magnitude upon reversing the magnetic

Significance

Photomagnetoresistance is a physical effect that describes the transport property of photocarriers under a magnetic field. We study the photomagnetoresistance in the van der Waals heterojunctions of WSe$_2$/quasi-two-dimensional electron gas on SrTiO$_3$. The coexistence of giant positive magnetoresistance (PMR) and negative magnetoresistance (NMR) is observed in a single device. The photomagnetoresistance reaches an extremely high level comparable with conventional magnetoresistance, with PMR and NMR peaking at 4,900,000% and −99.8%, respectively. The magnetoresistance spans over two orders of magnitude on inversion of magnetic field direction, implying a giant unidirectional magnetoresistance. Such a physical effect, referred to as giant bipolar unidirectional photomagnetoresistance, originates from the combined effect of strong out-of-plane spin polarization, magnetic field–enhanced recombination of photocarriers, and the Zeeman effect.

[1]To whom correspondence may be addressed. Email: jyc@usts.edu.cn or chengwei.qiu@nus.edu.sg.

[2]Y.J., A.H., K.L., and J.Z. contributed equally to this work.

field, displaying a giant unidirectional magnetoresistance (UMR) effect. By adjusting the thickness of the WSe$_2$ layer, we achieve the maxima of PMR and NMR that are 4,900,000% and –99.8%, comparable with the highest values reported so far (18, 22, 39–42) [e.g., about 15,000,000% for PMR at 1.8 K in gray arsenic (42, 43) and about –99% for NMR at 2 K in CrI$_3$ (18, 41)]. Through theoretical and experimental studies, the GBU-PhMR can be attributed to the combined effect of strong out-of-plane spin splitting, magnetic field–enhanced recombination of photocarriers, and the Zeeman effect. This work explores the unique magnetic transport of photocarriers in a WSe$_2$/Q2DEG heterojunction and its potential applications in high-sensitivity spintronic devices.

Results and Discussion

Fig. 1A shows a schematic of WSe$_2$/Q2DEG heterostructure. Based on our recent work, the Ar$^+$ ion bombardment assistant (AIBA) method is used to fabricate the device (*SI Appendix*, Fig. S1) (38). We used the WSe$_2$ crystals with a 2H phase and the (100) STO substrates with a perovskite structure. After the AIBA fabrication, a vdW contact can be achieved at the edges of WSe$_2$ and Q2DEG in Fig. 1B. Due to the intrinsic p-type conduction of WSe$_2$, a p–n junction is formed at the interface of WSe$_2$ and Q2DEG. Fig. 1C shows the microscopic image of the WSe$_2$/Q2DEG heterojunction and its corresponding top-view schematic diagram for clarifying the geometry. Atomic force microscopy (AFM) is used to display the amplified image of the selected area in Fig. 1C, Inset. The thickness of the WSe$_2$ layer is about 40.3 nm, and the etching depth of STO is about 54.5 nm. A spherical aberration–corrected

scanning transmission electron microscopy (C$_s$-corrected STEM) is used to investigate the lattice structures of WSe$_2$ and STO. In Fig. 1D, the scanning transmission electron microscopy (STEM) image demonstrates the hexagonal symmetry of 2H-WSe$_2$, which is verified by its fast Fourier transform (FFT) pattern. Raman spectrum and mapping are applied to identify the two characteristic Raman peaks of WSe$_2$ and clarify the junction structure (*SI Appendix*, Fig. S2). Raman mapping is used to image the composition and structure of materials based on their characteristic Raman spectra. In *SI Appendix*, Fig. S2B, yellow, purple, and green correspond to the Raman vibration modes of Au electrode, WSe$_2$ and STO, respectively. During the fabrication of device, Ar$^+$ ion bombardment is an important step to construct the heterojunction. Such a technique can ablate the atoms randomly on the surface of a material, possibly causing lots of defects. It must increase the disorder of the WSe$_2$/STO interface. To clarify the role of Ar$^+$ ion bombardment, we probed the surface of STO etched by Ar$^+$ ion bombardment using C$_s$-corrected STEM in Fig. 1E. It is found that the etched STO surface is atomically uneven and cannot be rigorously terminated by the SrO or TiO$_2$ layer. There exist atomic defects and dislocations within a cell layer, causing the different property from the SrO or TiO$_2$ termination alone (44). Such a disordered surface will give rise to the Anderson localized states, which play an important role in determining the physical properties of the device (45).

For the vdW WSe$_2$/Q2DEG heterojunction, our recent work reported the phenomenon of chargeable photoconductivity (CPC) (46). The intrinsic heterojunction has a very large built-in barrier and a broad space charge region (SCR), making it insulating at low temperature. Based on these previous
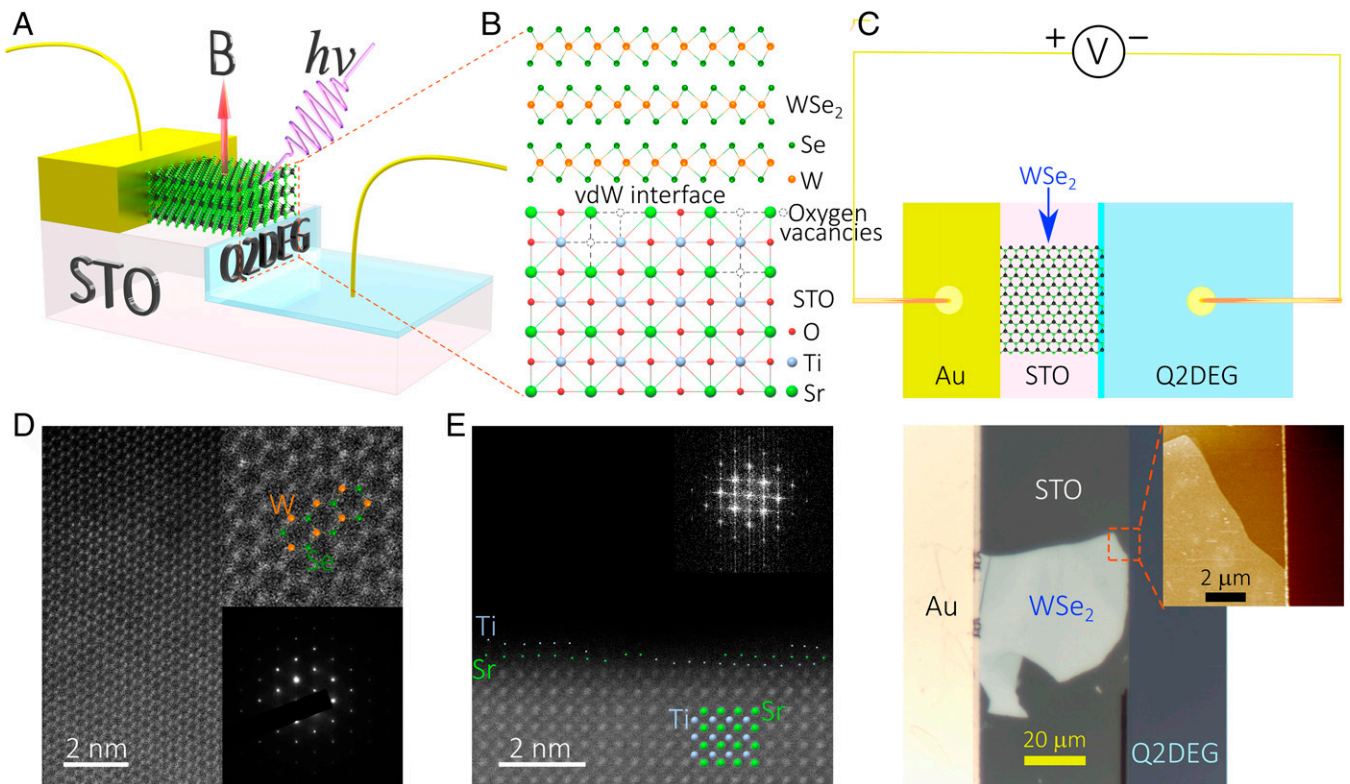

Fig. 1. Structure of the device. (A) Structural schematic of the WSe$_2$/Q2DEG heterostructure, showing the electric measurement under the magnetic field and light illumination. (B) Schematic diagram showing the vdW contact between WSe$_2$ and the oxygen-deficient STO surface. (C) Photograph of the WSe$_2$/Q2DEG heterojunction and the top view of the schematic diagram of the device for corresponding to its microscopic image. (C, Inset) AFM image illustrating magnification of the area near the interface. (D) A top-view STEM image of WSe$_2$ showing the 2H lattice structure. D, Inset is the FFT pattern of 2H-WSe$_2$. (E) Cross-sectional STEM image displaying the atomic defects and dislocations of the STO substrate etched by an Ar$^+$ beam. E, Inset is the FFT pattern of STO.

results, such an insulating device with high photosensitivity offers an opportunity to study the magnetic transport of photo-carriers without the interference from intrinsic carriers. In this work, we focus on the synergized effects of CPC and MR. Experimentally, the device is irradiated by 405-nm light to produce photocarriers, and a bias voltage (V_B) is applied to consume the stored charges. In dynamic balance, the device displays a stable current, accessible to the MR measurement. Fig. 2A shows the MR as a function of the magnetic field, demonstrating the different dependence on the positive and negative fields. Along the negative direction, the MR increases monotonously with the field, displaying giant PMR about 1,007.5%. However, the MR decreases greatly first and then, increases with the increase of the positive field. The largest NMR reaches −93.5% at a magnetic field of extremum ($B_e =$ 2.2 T). At 10 K, the device shows a coexistence of giant PMR and giant NMR accompanied by significant MR anisotropy depending on the sign of magnetic field, regarded as a GBU-PhMR effect. As is well known, the conventional MR materials usually exhibit the parity-symmetric field dependence of resistance. Distinctively, the GBU-PhMR device shows the unidirectional dependence of MR on the magnetic field. The MR spans over two orders of magnitude on inversion of field direction, implying a giant UMR (47). For comparison with other UMR systems, we plotted the UMR vs. field curve in Fig. 2A, Inset with the definition of UMR = [$R(B) - R(-B)$]/[$R(B) +$ $R(-B)$] × 100%. It is observed that the maximum UMR is over 95%, much higher than the other UMR materials reported recently.

The definition of MR is usually used for measuring the large PMR effect. However, for large NMR, it is difficult to implement a detailed description of the resistance decrease induced by magnetic field if the resistance drops over two orders of magnitude. Thus, such a definition is not appropriate for the GBU-PhMR effect with both giant PMR and NMR. Here, we use MR_{GBU} defined as $MR_{GBU} = R_j(B)/R_j(0)$, where R_j is the junction resistance, to describe the giant PMR and NMR together. It is PMR if $MR_{GBU} > 1$ or NMR if $MR_{GBU} < 1$. Fig. 2B shows MR_{GBU} as a function of the magnetic field (MR_{GBU}-B) at different temperatures. Above 30 K, the WSe$_2$/Q2DEG heterojunction exhibits a significant PMR effect. The MR_{GBU}-B curves display a symmetry with respect to $B = 0$ T, where MR_{GBU} at $+B$ is equal to that at $-B$. As the temperature falls down, PMR is drastically increased at $-B$, while NMR emerges at $+B$, demonstrating the transition from conventional PMR to GBU-PhMR. At 10 K, the NMR maximum reaches about −85.9% (or 0.14 in MR_{GBU}) at a magnetic field of extremum ($B_e \sim 3.2$ T). The NMR originates from the Zeeman effect, which is valid for a system with Anderson localized states (48). It is evident that Ar$^+$ ion bombardment, used for the fabrication of the WSe$_2$/Q2DEG heterojunction, gives rise to lots of atomic defects and dislocations (Fig. 1E). Also, Anderson localization plays an important role in determining the physical property of electron gas systems (49, 50), demonstrating the rationality of applying the Anderson localization model to interpret the NMR. Due to the strong spin-orbit coupling (SOC) of WSe$_2$, the spin polarization emerges and can be estimated by a related parameter (U_{sp}), which makes the symmetry center of the NMR curve shift along the negative direction of magnetic field (SI Appendix, Fig. S8 and section S5). U_{sp} can be obtained by $U_{sp} = \frac{1}{2m}\ln\frac{n_\uparrow}{n_\downarrow}$ (SI Appendix, section S3), where m is a fitting parameter and $n_\uparrow$ and $n_\downarrow$ are the percentages of spin-up and spin-down carriers in the total number, respectively. U_{sp} is used to compare experimental data with theoretical
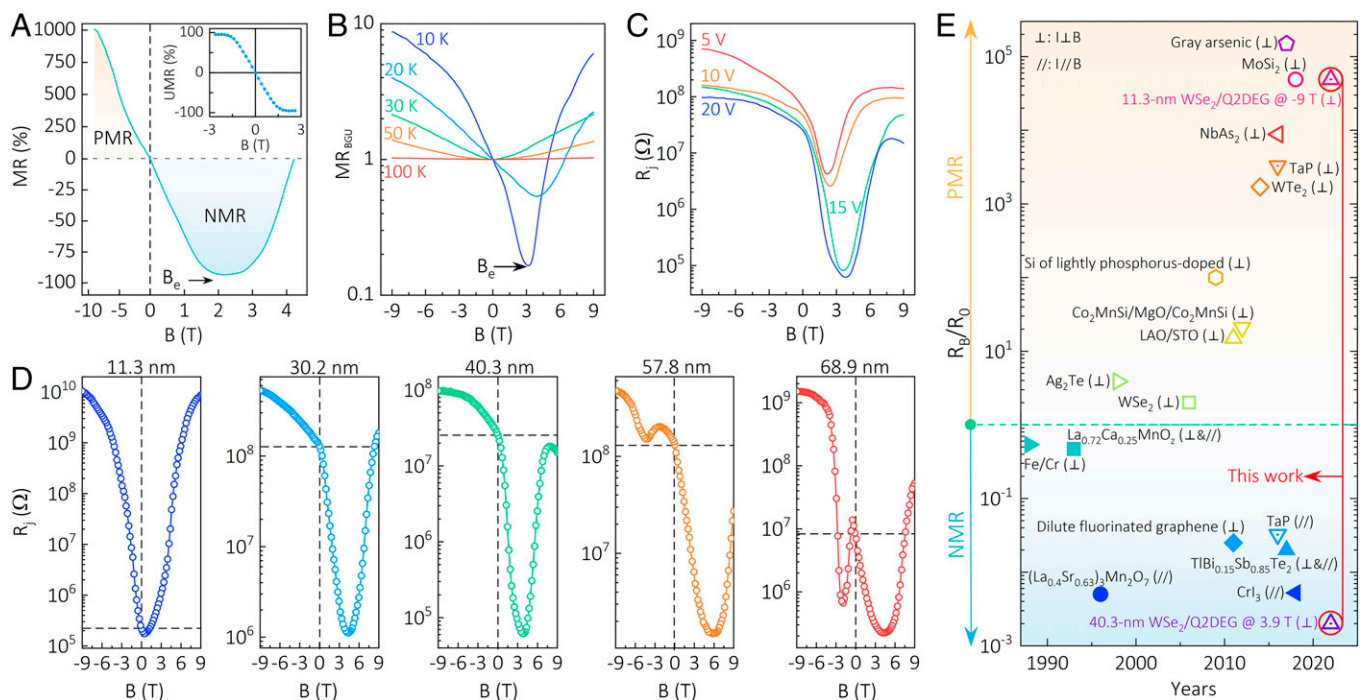

Fig. 2. GBU-PhMR. (A) Magnetic field dependence of MR at a bias voltage of 5 V, a temperature of 10 K, and continuous 405-nm optical illumination of 0.07 mW·cm^{-2}, where the different scales for positive and negative coordinates are used for a detailed description of giant PMR and NMR. (A, Inset) UMR vs. field. (B) MR_{GBU} as a function of the magnetic field at different temperatures under 2.1 mW·cm^{-2}. (C) R_j–B curves at various bias voltages at 10 K and $P_{opt} =$ 0.07 mW·cm^{-2}. (D) Dependence of R_j–B curves on WSe$_2$ thickness with $P_{opt} = 0.07$ mW·cm^{-2}. All samples were tested at $V_B = 20$ V and T = 10 K. (E) A comparison of PMR and NMR of some well-known spintronic materials over four decades; 11.3- and 40.3-nm WSe$_2$/Q2DEG heterojunctions exhibit the giant PMR and NMR, respectively, comparable with those classic PMR and NMR materials. The symbols ⊥ and // show the current perpendicular and parallel to the magnetic fields, respectively. NMR, negative magnetoresistance. LAO, LaAlO$_3$.

simulation for convenience. The existence of spin polarization causes the NMR to be shadowed by the PMR in negative fields. Therefore, the NMR can be observed only in positive fields.

Considering the bias dependence of R_j in a p–n junction, we investigated the relation between magnetoresistance and bias voltage in WSe$_2$/Q2DEG heterojunctions. In Fig. 2C, the R_j–B curves show that the NMR effect is prominently enhanced by increasing the bias voltage at $P_{opt} = 0.07$ mW·cm^{-2}. The largest MR reaches as high as –99.8%. At the same time, B_e changes from 2.2 to 3.9 T, with V_B increasing to 20 V. Fig. 2D shows the R_j–B curves with different thicknesses of WSe$_2$. The devices with thinner WSe$_2$ layers enable to display of larger PMR, while NMR becomes more pronounced in the thicker ones. Among them, the R_j–B curve of the 11.3-nm device exhibits the largest PMR value and the approximate parity symmetry with respect to $B = 0$ T, displaying a slight deviation of 0.5 T. The magnetic field induces an increase of R_j over four orders of magnitude, where $MR = 4,900,000\%$. With the WSe$_2$ layer thicker than 30 nm, the NMR effect emerges at $+B$, and the R_j–B curves lose the symmetry. In the 40.3-nm sample, the NMR value reaches its maximum at 3.9 T, where $MR = $ –99.8%. As the thickness increases, the NMR at $-B$ reveals a significant enhancement but tends to decrease at $+B$. In the 68.9-nm sample, the NMR value at $-B$ reaches a close level to that at $+B$. Here, the PMR cannot shadow the NMR in negative fields because of small U_{sp}. The observed thickness dependence of GBU-PhMR can be interpreted through the competition between PMR and NMR (*SI Appendix*, section S5). For the consistency of experimental results, we use the 40.3-nm sample to perform the following experiments. In general, both PMR and NMR shown in the GBU-PhMR device are quite impressive, compared with other well-known materials with large PMR (9, 19, 22, 39, 42, 43, 51–53) and NMR (4, 18, 40, 41, 54–57) (Fig. 2E). Based on the experimental results, it is found that that the parity symmetry of R_j–B curves is accompanied by PMR but fades away with the advent of NMR. This suggests that the PMR and NMR effects arise from different mechanisms with distinct dependence on the magnetic field.

Fig. 3A shows the charge distribution in SCR under continuous light illumination and bias voltage. Given the lateral junction geometry, large SCR makes the WSe$_2$ multilayer turn into planar electrified layers. The internal electric field (E_{in}) may affect the bottom transport WSe$_2$ layer, inducing spin polarization from strong SOC. For WSe$_2$ with strong intrinsic SOC, the UMR-type magnetic transport should be correlated with the spin-momentum locking. Fig. 3B shows the band structures of the WSe$_2$ bilayer with SOC considered at $E_{in} = 0.2$ V·nm^{-1}. By density functional theory (DFT) calculations, we note that E_{in} induces a huge Zeeman-type spin splitting among the top valence bands in the vicinity of K points, where its energy order increases up to 125 meV with E_{in}. With the space reversal symmetry broken by E_{in}, SOC tends to lift the spin degeneracy, but there is no significant spin splitting around Γ-point. So, the Rashba effect is negligible in WSe$_2$, especially compared with the Zeeman-type spin splitting (58). Around K point, the spin polarizations are out of plane and have opposite signs. The E_{in}-induced spin splitting is further studied in the mono- to quadlayers of WSe$_2$ under the electric fields of 0 to 0.5 V·nm^{-1} (*SI Appendix*, Figs. S3 and S4 and section S1). Since the spin-up band is closer to the Fermi level, the carriers, generated by light, prefer to have upward spin polarization, displaying the spin-up polarization. Such a spin polarization is perpendicular to the WSe$_2$ plane, thereby inducing the out-of-plane UMR (58). This is verified by the high asymmetry of R_j–B curves (Fig. 2). In addition, we used unpolarized light to generate photocarriers, which rules out the valley-spin effect

(59). For the WSe$_2$ film with $\sim$20 to 100 layers, the valley-spin effect is too weak to have a significant effect on the electronic transport (60). The Rashba effect is irrelevant owing to its tendency to the in-plane spin polarization (61). Additionally, the magnetism of the oxygen-deficient STO surface is also investigated at 5 K in *SI Appendix*, Fig. S5. It exhibits a very weak persistent magnetic moment with the coercive field less than 0.02 T, which is insufficient to induce such a giant UMR. Therefore, after a thorough analysis, we attribute the UMR effect to the E_{in}-induced Zeeman-type spin splitting.

Our recent study has demonstrated that the WSe$_2$/Q2DEG heterojunction on STO is the first system that exhibits the CPC effect (46). During the optical illumination, the device enables the coexistence of photoelectric conversion and storage in a single device. Fig. 3C shows the schematic diagram of carrier distribution at the interface of WSe$_2$ and Q2DEG before and after an optical illumination. The intrinsic heterojunction has a very wide SCR that causes a large barrier to block the electric transport. During the optical charging, the SCR is filled with photocarriers and stores them forever. The photocarriers stored in the SCR can recombine only when applying a bias voltage, regarded as a discharge process. A large photocurrent is released during the discharge. With the stored photocarriers depleted, the device recovers to the insulating state. In our experiments, to reach the full optical charging, the device was irradiated by a 405-nm laser with $P_{opt} = 16$ mW·cm^{-2} for 7 s. Fig. 3D shows the current vs. voltage (I-V) loops in darkness at 0 T after full optical charging with/without the magnetic field applied. There is no difference between them. The magnetic field cannot affect the charging process and charge capacity of the device. As we have known, the photocarriers are the light-created holes stored stably in the SCR of WSe$_2$ (46). Due to the high built-in barrier at the interface, the random thermal motions of the light-created holes are confined to the SCR. A magnetic field can deflect the trajectories of those light-created holes. However, there are no free electrons in this region, so no electron-hole recombination happens without bias voltage applied. Therefore, the photocarrier capacity cannot be changed by the magnetic field. A complete I-V loop in a CPC device contains the forward (voltage increase) and backward (voltage decrease) curves. The forward curve shows a releasing process of photocarriers, and the backward one reveals a recovery process toward the intrinsic insulating state. It is concluded that the bias voltage tends to drive the photocarriers to recombine, causing the depletion of photocarriers stored in SCR. For the case in Fig. 2, continuous light irradiation and stable current result in a dynamic equilibrium between generation and recombination of photocarriers. Actually, the magnetic field should affect the releasing process of photocarriers stored in SCR. Fig. 3E and F shows the semilog I-V loops of the WSe$_2$/Q2DEG heterojunction under positive and negative magnetic fields after full optical charging, respectively. The I-V loops of the linear coordinate are exhibited in *SI Appendix*, Fig. S6A. For a p–n junction, there exists a turn-on voltage (V_{on}) in its I-V characteristics, above which the current will increase greatly. It is noted that the magnetic field induces a shift of V_{on} in backward curves. Under the negative magnetic field, V_{on} grows monotonously as B increases, which corroborates the positive impact of B on the photocarrier recombination. Under the positive magnetic field, with its size large enough (>3 T), the NMR cannot cancel out the impact of PMR, still causing V_{on} to increase. The shift of V_{on} reflects the change of built-in potential. Additionally, for a CPC device, the built-in potential is determined by the density of stored photocarriers in SCR. The photocarriers stored at deeper regions of SCR are
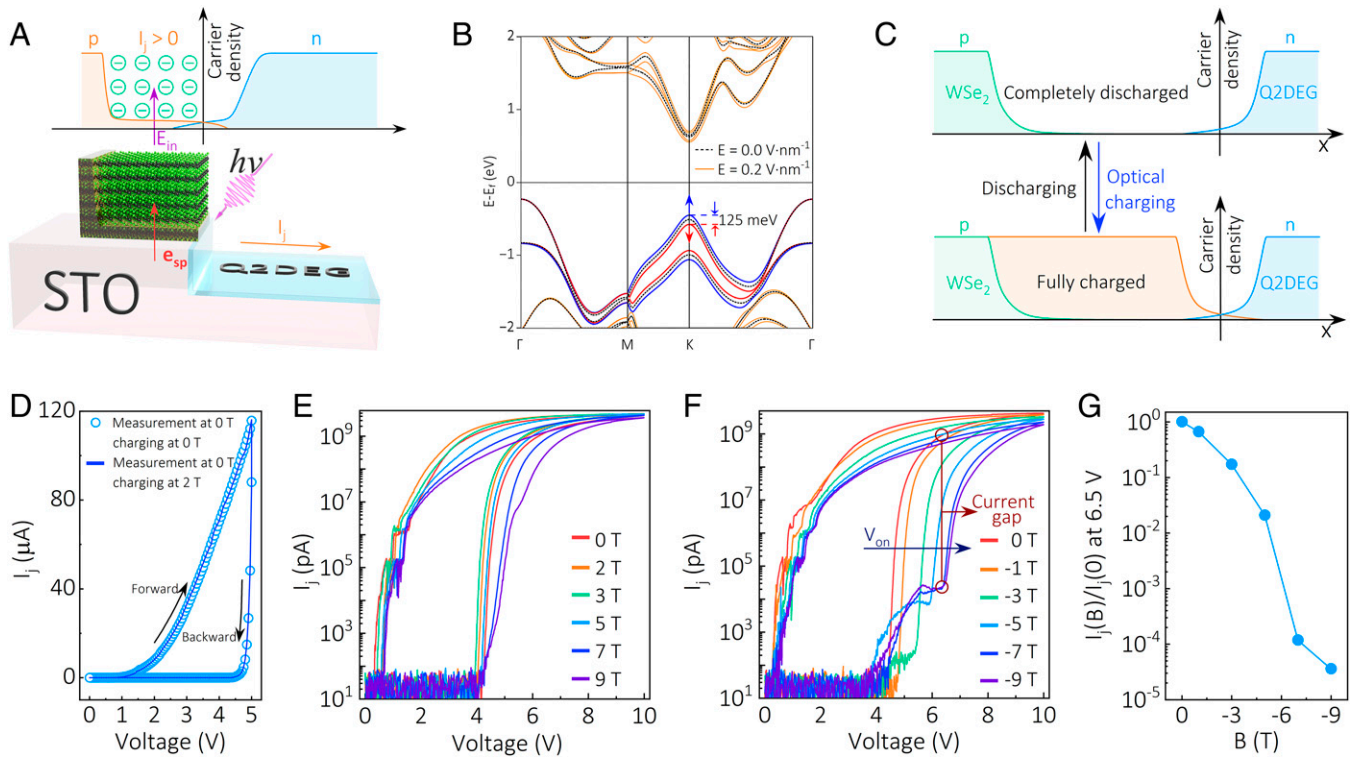
Fig. 3. Origins of UMR and giant PMR. (*A*) Schematics of the photocarrier distribution in SCR with the current across the junction under continuous light illumination and bias voltage, where $\vec{e}_{sp}$ shows the direction of spin polarization. (*B*) Band structures of a bilayer WSe$_2$ with (solid lines) and without (dotted lines) electric fields. Blue and red emphasize the bands of out-of-plane spin-up and spin-down polarizations, respectively. (*C*) Schematic diagram showing carrier distribution at the interface of WSe$_2$ and Q2DEG with optical charging and discharging. (*D*) I-V loops measured in darkness without the magnetic field at 10 K after full optical charging at 0 and 5 T. Semilog I-V loops measured in darkness by applying positive (*E*) and negative (*F*) magnetic fields after full optical charging. (*G*) $I_j(B)/I_j(0)$ as a function of magnetic field at the bias voltage of 6.5 V. The data points are picked from the backward curves in *F*.

further depleted by the high field during the electronic transport (*SI Appendix*, Fig. S6B and section S2). Therefore, the magnetic field dependence of V_{on} results from the field-enhanced recombination of photocarriers. Near V_{on}, the device exhibits the highest sensitivity to the magnetic field, displaying a very large current gap up to five orders of magnitude (Fig. 3G). The above process has been recognized experimentally as the giant PMR effect. A reasonable explanation is that the Lorentz force causes the helical motion of photocarriers under the magnetic field, substantially increasing their travel distances during the electric transport. It increases the probability of electron-hole recombination greatly, and that causes the depletion of deeply stored photocarriers.

Light-tunable MR is an intriguing and challenging field, where despite some progress, the effect of light on MR is dully small (62, 63). The experimental data in Fig. 4A–C demonstrates that the NMR effect is greatly controlled by the light intensity. Near B_e, the light induced by the MR_{GBU} transverses over two orders of magnitude, resulting from the optical tuning of E_{in}. With P_{opt} increasing, more photocarriers are produced and stored into SCR, causing a thinner electrified layer and smaller E_{in}. Given the strong dependence of spin polarization on E_{in}, the decrease of E_{in} will lower the concentration of spin-up carriers and reduce the value of U_{sp}, thereby suppressing the NMR effect. Actually, the Zeeman effect determined by both spin polarization and magnetic field should be responsible for the NMR effect. This type of Zeeman NMR shows a strong dependence on the U_{sp} (*SI Appendix*, section S3). Similarly, the increase of the light wavelength also weakens the GBU-PhMR effect (*SI Appendix*, Fig. S7). It is worth pointing out that there is an optimal optical power density (P_{max}) value to maximize the NMR effect at a selected bias voltage. In Fig. 4D, *Inset*,

$1/P_{max}$ shows the linear dependence on the bias voltage. For the CPC device, reported by our recent work, the bias increase drives more stored photocarriers to participate in the electric transport (46). Additionally, the increase of P_{opt} raises the density of photocarriers, so we have the relation as (*SI Appendix*, section S4)

$$(V_B - V_0) \cdot P_{opt} \propto n_s, \qquad [1]$$

where V_B is the bias voltage, V_0 is a fitting parameter, and n_s is the sheet carrier density in the SCR of WSe$_2$. Considering the inversely proportional relation between P_{opt} and V_B, the data points in Fig. 4D, *Inset* correspond to almost the same value of n_s, implying that n_s determines the maximum NMR. It is n_s that plays a dominant role in the NMR but not light intensity alone. There is an optimal photocarrier density that maximizes the extremum value of NMR in positive fields. Based on Eq. 1, we can interpret the different light intensity dependence of the MR_{GBU}–B curves in Fig. 4A–C. For the relatively small bias voltage of 10 V in Fig. 4A, the light intensity needs to increase to make n_s close to the optimal value, so the extremum value of NMR increases with the increase of light intensity. The maximum of the NMR extremum is obtained at $P_{opt} = 0.67$ mW/cm^2. With P_{opt} increasing to 2.1 mW/cm^2, n_s deviates from the optimal value, causing the decrease of the NMR extremum. For the case of $V_B = 15$ V in Fig. 4B, the similar physical process is also observed. The NMR extremum first increases and then decreases with the increase of light intensity, and it reaches the maximum at $P_{opt} = 0.15$ mW/cm^2. For the large-enough bias voltage ($V_B = 20$ V) in Fig. 4C, the light intensity must be decreased to make n_s close to the optimal value, causing the
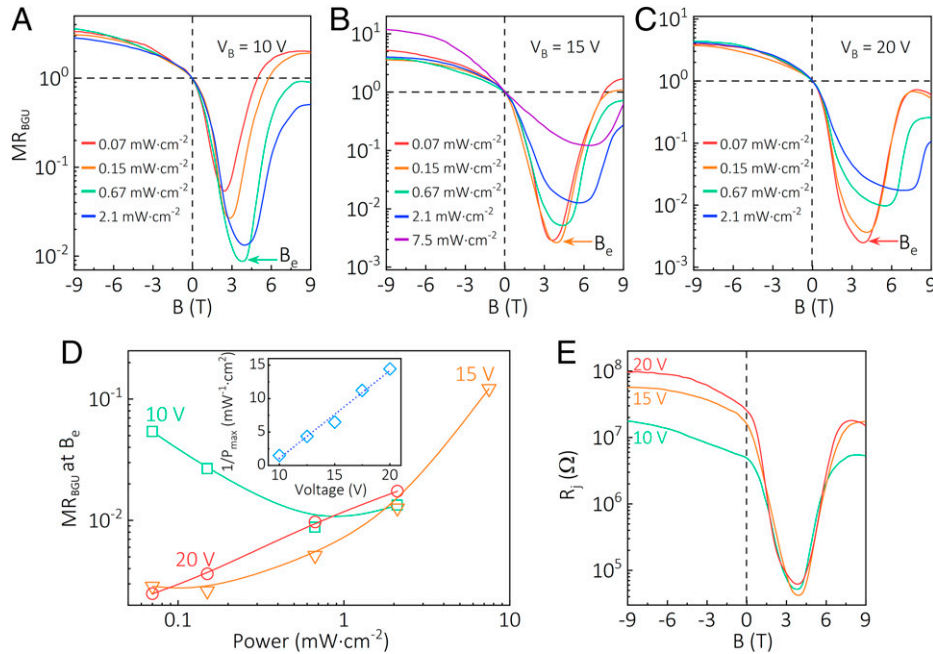
Fig. 4. Light-tunable GBU-PhMR. Field dependence of MR_{GBU} under 405-nm optical illumination with various P_{opt} at (A) $V_B = 10$ V, (B) $V_B = 15$ V, and (C) $V_B = 20$ V. (D) MR_{GBU} at B_e as a function of P_{opt} at different bias voltages. D, Inset is the linear dependence of $1/P_{max}$ on the bias voltage. (E) R_j–B curves by applying bias voltages and optical illuminations with their corresponding P_{max}, where P_{max} is 0.67 mW·cm^{-2} at 10 V, 0.15 mW·cm^{-2} at 15 V, and 0.07 mW·cm^{-2} at 20 V.

monotonous decrease of the NMR extremum as P_{opt} increases. Also, we can interpret the role of bias voltage in modulating the NMR based on the same mechanism in Fig. 2C. For small P_{opt} of 0.07 mW/cm^2, the initial photocarrier density is lower than the optimal value. Bias voltage needs to increase to make the photocarrier density close to the optimal value, so the extremum value of NMR increases with the increase of bias voltage. Fig. 4E shows R_j–B curves by selecting appropriate bias voltages and their corresponding P_{max}. All of the R_j–B curves exhibit almost the same B_e, despite different V_B and P_{opt}, still attributed to the same optimal photocarrier density. By analyzing the experimental results in Figs. 2–4, we realize that the observed GBU-PhMR effect is determined by the competition between PMR and NMR. A theoretical model has been proposed to describe the dependence of junction resistance on the magnetic field in *SI Appendix*, section S5. The change of junction resistance can be written as

$$\Delta R_{GBU-PhMR}(B) = \Delta R_{PMR}(B) + \Delta R_{NMR}(B) = C_1 |B|^\alpha$$
$$+ \frac{C_2}{\exp[m(B+U_{sp})] + \exp[-m(B+U_{sp})]},\quad [2]$$

where ΔR_{PMR} and ΔR_{NMR} are the resistance changes caused by PMR and NMR, respectively, and α, C_1, and C_2 are fitting parameters. Here, the value of C_1/C_2 can describe the competition between PMR and NMR. A large value of C_1/C_2 indicates the dominant role of PMR in the magnetic transport; otherwise, the NMR dominates. Based on this model, the simulation of the GBU-PhMR effect is shown in *SI Appendix*, Fig. S8, consistent with the experimental results.

To clarify the spin polarization, we investigated the dependence of MR on the angle (θ) between B and $\vec{e}_{sp}$ as shown in Fig. 5A. The limitation of the physical property measurement system (PPMS) makes it impossible for the device to rotate in a magnetic field and to be exposed to the stable optical illumination at the same time. In *SI Appendix*, Fig. S6B, it is noted that even though most of the photocarriers tend to recombine in

the magnetic field of 9 T, there still remain a few inert photocarriers to cause nanoamp-level current in the darkness for a longtime. This allows us to achieve the measurements of I_j–θ relations in different magnetic fields. In this case, the MR effect mainly results from the scattering response to the magnetic field without photocarrier recombination. Fig. 5A, Inset is a schematic showing the angle (θ) between B and the z axis. With $\theta = 0°$ and 180°, the device exhibits the significant NMR and PMR effects, respectively. With $\theta = 90°$ and 270°, I_j is independent of B. It suggests that the electronic transport cannot be influenced by the component of the magnetic field perpendicular to $\vec{e}_{sp}$ when the field rotates in a plane perpendicular to the current. Here, I_j exhibits the unidirectional dependence on the external magnetic field, which is identified as the UMR effect. Another intriguing observation is that the shape of I_j–θ curve is correlated with the magnitude of magnetic field. Below 5 T, I_j decreases monotonously with θ in the range from 0° to 180°, while with B increasing over 5 T, it decreases first and then increases with θ. Fig. 5B shows the curve of $I_j(B)/I_j(0)$ vs. B with different θ, where $I_j(B)$ and $I_j(0)$ are the junction currents with and without magnetic field applied. With $\theta = 90°$, there is no significant MR in the device, agreeing with the result in Fig. 5A. With $\theta = 0°$ and 45°, $I_j(B)$ increases monotonically with positive field, but it decreases first and then increases along the negative field. This implies that $I_j(B)$ is determined by $B + U_{sp}$. Along the positive direction, B is parallel to $\vec{e}_{sp}$, causing the monotonic increase of $I_j(B)$ with B. Along the negative direction, the external magnetic field needs to compete with the spin polarization. The value of $B + U_{sp}$ first decreases with B and then, with $|B| > U_{sp}$, it increases with B. Thus, $I_j(B)$ exhibits a nonmonotonic dependence on the external magnetic field. Fig. 5C shows I_j as a function of the magnetic field along the x axis, where B is parallel to I_j. It is observed that the R_j–B curve exhibits a parity symmetry to $B = 0$ T, demonstrating that $\vec{e}_{sp}$ is parallel to the z axis. The I_j maximum is obtained at 9 T without competition between NMR and PMR. In this case, the PMR effect almost disappears with the magnetic field parallel to the current
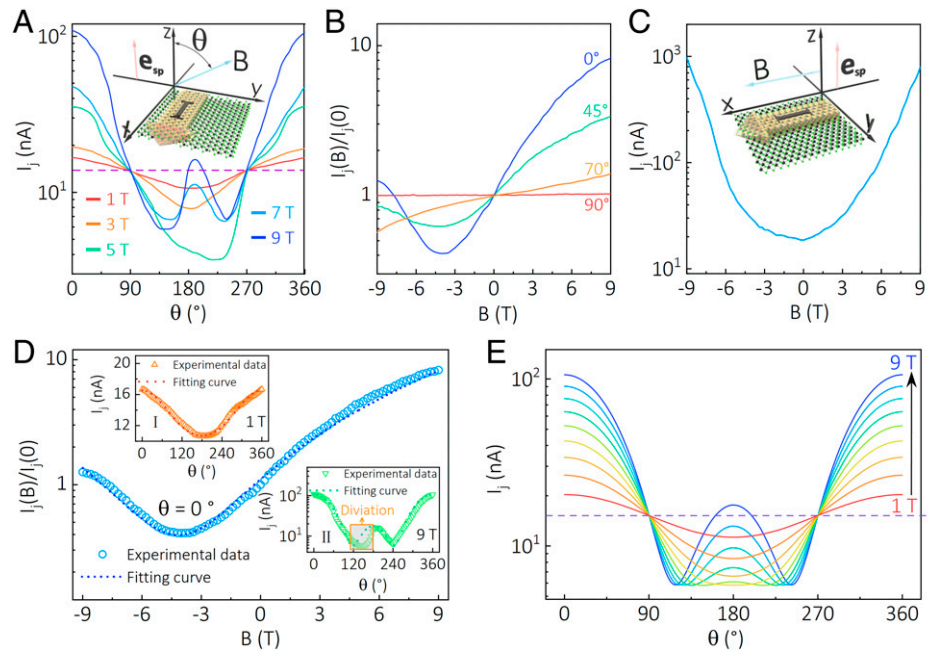
Fig. 5. Anisotropy and mechanism of NMR. (*A*) I_j as a function of θ under different magnetic fields in darkness at 6 V and 10 K. *A, Inset* is a schematic showing the angle (θ) between *B* and the *z* axis. I_j and $\vec{e}_{sp}$ are along the *x* and *z* axes, respectively. (*B*) $I_j(B)/I_j(0)$ vs. *B* measured at $\theta = 0°$, $45°$, $70°$, and $90°$. (*C*) I_j–*B* characteristic under optical illumination of 0.1 mW·cm^{-2} at 6 V and 10 K. *C, Inset* shows that *B* is parallel to the I_j direction. (*D*) Experimental data vs. fitting curve showing $I_j(B)/I_j(0)$ as a function of *B*. *D, Insets I and II* are I_j–θ curves at 1 and 9 T, respectively, obtained by experiment and fitting. (*E*) Theoretical simulation of I_j–θ curves in the field range of 1 to 9 T, showing the resist of spin polarization against the external magnetic field.

direction. We have known that the increase of the carrier transport path, caused by Lorentz force, enhances the recombination of electron-hole pairs, causing large PMR. However, with *B* parallel to the current direction, no Lorentz force exists for the moving carriers, preventing the PMR effect. By investigating I_j in different field directions, it is evident that the field dependence of NMR is determined not only by the angle between $\vec{B}$ and $\vec{e}_{sp}$ but also, by the angle between *B* and I_j.

A theoretical model is proposed to explain the highly anisotropic NMR effect (*SI Appendix*, section S3). In Fig. 5*D*, we simulate $I_j(B)/I_j(0)$ as a function of *B*, showing the good agreement with the experimental data. It is reasonable to ascribe large NMR to the Zeeman effect (62). In Fig. 5*D, Insets I and II*, the fitting curves exhibit θ dependences of I_j at 1 and 9 T, respectively, agreeing with the experimental data. With U_{sp} equal to 3.9 T, we can calculate the value of $n_\uparrow/n_\downarrow$ (~1.73), corresponding to $n_\uparrow \sim 63.3\%$. It is worth pointing out that there is some deviation between theoretical and experimental values in the range of 120° to 180° at 9 T (Fig. 5*D, Inset II*). This results from the MR hysteresis during the rotation of the magnetic field. The spin polarization is controlled not only by E_{in} but also, by the external magnetic field. Spin rotation lags behind the external magnetic field, thus causing MR hysteresis. With θ increasing from 0° to 90°, the external magnetic field enhances the spin-up polarization, inducing larger U_{sp}. When the field rotates in the range from 90° to 180°, the component of *B* along the *z* axis (B_z) will be antiparallel to $\vec{e}_{sp}$. A larger B_z is required to balance larger U_{sp}. So, the current minimum moves to a higher angle, causing deviation from the theoretical value. To verify the hysteresis of MR, we investigate the R_j–*B* loops at different P_{opt} (*SI Appendix*, Fig. S9), demonstrating that the hysteresis effect mainly occurs in the NMR region. In Fig. 5*E*, we simulate the θ-dependence of R_j at different *B*. With $B < 4$ T, B_z is smaller than U_{sp} at all angles, and I_j exhibits a cosine-like dependence on θ. With *B* increasing over 5 T, the size of B_z will exceed U_{sp} near $\theta = 180°$. Spin-down

photocarriers start to make the main contribution to NMR, thus displaying an anomalous increase of I_j.

In summary, we have observed a GBU-PhMR effect in WSe$_2$/Q2DEG heterojunctions, which reflects the intricate relationship between optical and magnetic transport properties. Based on our experimental and theoretical research, it is concluded that the GBU-PhMR effect originates from the combined action of out-of-plane spin splitting, magnetic field–enhanced recombination of photocarrier, and the Zeeman effect. The spin polarization leads to the unidirectional dependence of scattering on the magnetic field, explaining the UMR effect. The PMR effect, caused by the field-induced photocarrier recombination, is described by an R_j–*B* curve with symmetry to $B = 0$ T, showing the competition with the NMR effect. The Zeeman effect is responsible for the anisotropic giant NMR that breaks the symmetry of R_j–*B* curve. When the WSe$_2$/Q2DEG heterojunction shows the unique magnetooptical transport, all the above mechanisms work simultaneously and contribute to the GBU-PhMR effect. In addition, the light tuning can cause a change in MR over two orders of magnitude. A theoretical model is proposed to explain the anisotropic MR response, aligning with the experimental data. Our work opens up the opportunities to achieve high-performance light-tunable spintronic devices.

Methods

Sample Fabrication. High-quality 2H-WSe$_2$ single-crystal bulk and (100) STO substrates were purchased from Nanjing Muke Nano Technology Co., Ltd. and Hefei Kejing Materials Technology Co., Ltd. The WSe$_2$/Q2DEG heterojunction is prepared by the AIBA method (*SI Appendix*, Fig. S1) based on our recent work (38, 46). WSe$_2$ flakes were mechanically exfoliated from a piece of bulk single crystal onto STO substrates. Through a lithographic technique, a half of the WSe$_2$ flake was coated by photoresist, and the other half was exposed to air. Then, an Au electrode was deposited on the sample by magnetron sputtering, and the photoresist was removed by acetone. After that, the lithographic technique was used again to cover the part of the WSe$_2$ flake contacting the Au electrode and to leave the square area containing bare STO and WSe$_2$. The sample was

irradiated for 3 min by an Ar$^+$ ion beam with a beam voltage of 400 V. A water-cooled sample holder was used during the etching process. Using the above AIBA method, the WSe$_2$/Q2DEG heterojunctions were successfully fabricated after removing photoresist with acetone.

Characterization. Multilayer WSe$_2$ flakes are identified by an optical microscope. AFM was used to determine the thickness of the samples and their surface morphology. C$_s$-corrected STEM is used to investigate the lattice structure of WSe$_2$ and STO. Micro-Raman spectroscopy was used to analyze the WSe$_2$/Q2DEG heterojunctions under ambient conditions. Nonpolarized and off-resonance Raman spectra and mapping are measured with a 532-nm excitation laser.

Electrical Measurement. R_j was measured by a standard two-probe method using Keithley 2400 and 6517B Source Meters. Photoelectric and photomagnetoresistance measurements were performed in the PPMS (Quantum Design) with an He atmosphere. Power-tunable light, supplied by several semiconductor lasers with wavelengths of ~405 to 808 nm, was transmitted into the sample chamber through an optical fiber bundle.

Electronic Structure Calculations. The electronic structure calculation with the SOC included was performed within DFT using the Vienna ab initio simulation package (VASP) (64, 65). The Perdew–Burke–Ernzehorf (PBE) (66) exchange-correlation functional is used throughout after negligible difference in the electronic structure was found between the Perdew–Zunger (67) and PBE. The projector augmented-wave datasets (68) of the PBE type for W and Se with a plane wave energy cutoff of 500 eV were used. Bulk 2H-WSe$_2$ has space group P6$_3$/mmc (194) with lattice constant a = 3.283 Å and c = 12.960 Å (69, 70). The layered systems were using the same lattice constant (no geometry optimization was performed). We applied an electric field perpendicular to the (001) surface to the few-layer structures using dipole sheets in the middle of vacuum regions implemented in VASP (71). The vacuum region was large enough (about 32 Å for bilayer) to avoid artificial interactions in a periodic system. The Brillouin zone was sampled with a Monkhorst–Pack grid of size 12 × 12 × 1 (72). K path along high-symmetry points was shown for band structure calculations as depicted in *SI Appendix*, Fig. S3.

Data Availability. All study data are included in the article and/or *SI Appendix*.

Author affiliations: ^{a}Jiangsu Key Laboratory of Micro and Nano Heat Fluid Flow Technology and Energy Application, School of Physical Science and Technology, Suzhou University of Science and Technology, Suzhou 215009, China; ^{b}Department of Applied Physics, Nanjing University of Science and Technology, Nanjing 210094, China; ^{c}Department of Electrical and Computer Engineering, National University of Singapore, 117583 Singapore; ^{d}International Collaborative Laboratory of 2D Materials for Optoelectronics Science and Technology of Ministry of Education, Institute of Microscale Optoelectronics, Shenzhen University, Shenzhen 518060, China; ^{e}School of Materials Science and Engineering, Shanghai University, Shanghai 200444, China; ^{f}Macau Institute of Systems Engineering, Macau University of Science and Technology, Macau 999078, China; ^{g}School for Optoelectronic Engineering, Zaozhuang University, Shandong 277160, China; ^{h}Department of Chemistry, National University of Singapore, 117543 Singapore; ^{i}Centre for Advanced 2D Materials, National University of Singapore, 117543 Singapore; and ^{j}Department of Physics, National University of Singapore, 117543 Singapore

Author contributions: Y.J. and C.-W.Q. designed research; Y.J., A.H., K.L., and J.Z. performed research; Y.J. and A.H. contributed new reagents/analytic tools; Y.J., A.H., K.L., J.Z., G.L., R.Z., Q.Z., Z.W., C.Z., L.W., Y.Q., J.G., K.P.L., and A.T.S.W. analyzed data; and Y.J., A.H., K.L., and C.-W.Q. wrote the paper.

1. A. B. Pippard, *Magnetoresistance in Metals* (Cambridge University Press, 1989).
2. G. Giuliani, A general law for electromagnetic induction. *Europhys. Lett.* **81**, 60002 (2008).
3. N. W. Ashcroft, N. D. Mermin, *Solid State Physics* (Holt, Rinehart and Winston, New York, NY, 1976).
4. M. N. Baibich et al., Giant magnetoresistance of (001)Fe/(001)Cr magnetic superlattices. *Phys. Rev. Lett.* **61**, 2472–2475 (1988).
5. B. Dieny et al., Giant magnetoresistive in soft ferromagnetic multilayers. *Phys. Rev. B Condens. Matter* **43**, 1297–1300 (1991).
6. J. C. Rife et al., Design and performance of GMR sensors for the detection of magnetic microbeads in biosensors. *Sens. Actuators A Phys.* **107**, 209–218 (2003).
7. R. S. Gaster et al., Quantification of protein interactions and solution transport using high-density GMR sensor arrays. *Nat. Nanotechnol.* **6**, 314–320 (2011).
8. B. Baek, W. H. Rippard, S. P. Benz, S. E. Russek, P. D. Dresselhaus, Hybrid superconducting-magnetic memory device using competing order parameters. *Nat. Commun.* **5**, 3888 (2014).
9. M. P. Delmo, S. Yamamoto, S. Kasai, T. Ono, K. Kobayashi, Large positive magnetoresistive effect in silicon induced by the space-charge effect. *Nature* **457**, 1112–1115 (2009).
10. G. Schmidt et al., Large magnetoresistance effect due to spin injection into a nonmagnetic semiconductor. *Phys. Rev. Lett.* **87**, 227203 (2001).
11. C. L. Chien, J. Q. Xiao, J. S. Jiang, Giant negative magnetoresistance in granular ferromagnetic systems. *J. Appl. Phys.* **73**, 5309–5314 (1993).
12. H. Li et al., Negative magnetoresistance in Dirac semimetal Cd$_3$As$_2$. *Nat. Commun.* **7**, 10301 (2016).
13. T. Valet, A. Fert, Theory of the perpendicular magnetoresistance in magnetic multilayers. *Phys. Rev. B Condens. Matter* **48**, 7099–7113 (1993).
14. J. B. Goodenough, Theory of the role of covalence in the perovskite-type manganites [La, M(II)]MnO$_3$. *Phys. Rev.* **100**, 564–573 (1955).
15. Y. Tokura, Y. Tomioka, Colossal magnetoresistive manganites. *J. Magn. Magn. Mater.* **200**, 1–23 (1999).
16. J. Mathon, A. Umerski, Theory of tunneling magnetoresistance of an epitaxial Fe/MgO/Fe(001) junction. *Phys. Rev. B Condens. Matter Mater. Phys.* **63**, 220403 (2001).
17. M. Tanaka, Y. Higo, Large tunneling magnetoresistance in GaMnAs/AlAs/GaMnAs ferromagnetic semiconductor tunnel junctions. *Phys. Rev. Lett.* **87**, 026602 (2001).
18. T. Song et al., Giant tunneling magnetoresistance in spin-filter van der Waals heterostructures. *Science* **360**, 1214–1218 (2018).
19. H.-x. Liu et al., Giant tunneling magnetoresistance in epitaxial Co$_2$MnSi/MgO/Co$_2$MnSi magnetic tunnel junctions by half-metallicity of Co$_2$MnSi and coherent tunneling. *Appl. Phys. Lett.* **101**, 132418 (2012).
20. S. Maekawa, H. Fukuyama, Magnetoresistance in two-dimensional disordered systems: Effects of Zeeman splitting and spin-orbit scattering. *J. Phys. Soc. Jpn.* **50**, 2516–2524 (1981).
21. A. G. Aronov, S. Hikami, A. I. Larkin, Zeeman effect on magnetoresistance in high-temperature superconductors. *Phys. Rev. Lett.* **62**, 965–968 (1989).
22. M. N. Ali et al., Large, non-saturating magnetoresistance in WTe$_2$. *Nature* **514**, 205–208 (2014).
23. O. Pavlosiuk, P. Swatek, D. Kaczorowski, P. Wiśniewski, Magnetoresistance in LuBi and YBi semimetals due to nearly perfect carrier compensation. *Phys. Rev. B* **97**, 235132 (2018).
24. X. Huang et al., Observation of the chiral-anomaly-induced negative magnetoresistance in 3D Weyl semimetal TaAs. *Phys. Rev. X* **5**, 031023 (2015).
25. F. Arnold et al., Negative magnetoresistance without well-defined chirality in the Weyl semimetal TaP. *Nat. Commun.* **7**, 11615 (2016).
26. Y. Wang et al., Gate-tunable negative longitudinal magnetoresistance in the predicted type-II Weyl semimetal WTe$_2$. *Nat. Commun.* **7**, 13142 (2016).
27. A. K. Geim, I. V. Grigorieva, van der Waals heterostructures. *Nature* **499**, 419–425 (2013).
28. Y. Liu et al., van der Waals heterostructures and devices. *Nat. Rev. Mater.* **1**, 16042 (2016).
29. K. S. Novoselov, A. Mishchenko, A. Carvalho, A. H. Castro Neto, 2D materials and van der Waals heterostructures. *Science* **353**, aac9439 (2016).
30. S.-H. Bae et al., Integration of bulk materials with two-dimensional materials for physical coupling and applications. *Nat. Mater.* **18**, 550–560 (2019).
31. R. Xiang et al., One-dimensional van der Waals heterostructures. *Science* **367**, 537–542 (2020).
32. G. Hu et al., Topological polaritons and photonic magic angles in twisted α-MoO$_3$ bilayers. *Nature* **582**, 209–213 (2020).
33. J. Zhou et al., Large tunneling magnetoresistance in VSe$_2$/MoS$_2$ magnetic tunnel junction. *ACS Appl. Mater. Interfaces* **11**, 17647–17653 (2019).
34. Q. Zhu, M. W.-Y. Tu, Q. Tong, W. Yao, Gate tuning from exciton superfluid to quantum anomalous Hall in van der Waals heterobilayer. *Sci. Adv.* **5**, eaau6120 (2019).
35. P. Huang et al., Ultra-long carrier lifetime in neutral graphene-hBN van der Waals heterostructures under mid-infrared illumination. *Nat. Commun.* **11**, 863 (2020).
36. H. S. Lee, J. Ahn, W. Shim, S. Im, D. K. Hwang, 2D WSe$_2$/MoS$_2$ van der Waals heterojunction photodiode for visible-near infrared broadband detection. *Appl. Phys. Lett.* **113**, 163102 (2018).
37. J. Binder et al., Upconverted electroluminescence via Auger scattering of interlayer excitons in van der Waals heterostructures. *Nat. Commun.* **10**, 2335 (2019).
38. Y. Chen et al., A universal method to fabricate p-n or Schottky heterojunctions based on two-dimensional electron gas. *Appl. Phys. Lett.* **115**, 241603 (2019).
39. Z. Yuan, H. Lu, Y. Liu, J. Wang, S. Jia, Large magnetoresistance in compensated semimetals TaAs$_2$ and NbAs$_2$. *Phys. Rev. B* **93**, 184405 (2016).
40. Y. Moritomo, A. Asamitsu, H. Kuwahara, Y. Tokura, Giant magnetoresistance of manganese oxides with a layered perovskite structure. *Nature* **380**, 141–144 (1996).
41. Z. Wang et al., Very large tunneling magnetoresistance in layered magnetic semiconductor CrI$_3$. *Nat. Commun.* **9**, 2516 (2018).
42. M. Matin, R. Mondal, N. Barman, A. Thamizhavel, S. K. Dhar, Extremely large magnetoresistance induced by Zeeman effect-driven electron-hole compensation and topological protection in MoSi$_2$. *Phys. Rev. B* **97**, 205130 (2018).
43. L. Zhao et al., Magnetotransport properties in a compensated semimetal gray arsenic. *Phys. Rev. B* **95**, 115119 (2017).
44. S. N. Rebec et al., Dichotomy of the photo-induced 2-dimensional electron gas on SrTiO$_3$ surface terminations. *Proc. Natl. Acad. Sci. U.S.A.* **116**, 16687–16691 (2019).
45. S. A. Bilmes, P. Mandelbaum, F. Alvarez, N. M. Victoria, Surface and electronic structure of titanium dioxide photocatalysts. *J. Phys. Chem. B* **104**, 9851–9858 (2000).
46. Y. Jiang et al., Coexistence of photoelectric conversion and storage in van der Waals heterojunctions. *Phys. Rev. Lett.* **127**, 217401 (2021).
47. C. O. Avci et al., Unidirectional spin Hall magnetoresistance in ferromagnet/normal metal bilayers. *Nat. Phys.* **11**, 570–575 (2015).
48. H. Fukuyama, K. Yoshida, Negative magnetoresistance in the Anderson localized States. *J. Phys. Soc. Jpn.* **46**, 102–105 (1979).
49. I. Pallecchi et al., Giant oscillating thermopower at oxide interfaces. *Nat. Commun.* **6**, 6678 (2015).
50. L. J. Brillson, T. M. Levin, G. H. Jessen, F. A. Ponce, Localized states at InGaN/GaN quantum well interfaces. *Appl. Phys. Lett.* **75**, 3835–3837 (1999).

51. I. S. Chuprakov, K. H. Dahmen, Large positive magnetoresistance in thin films of silver telluride. *Appl. Phys. Lett.* **72**, 2165–2167 (1998).

52. S. Kunjachan, Positive magnetoresistance in $Ti_xW_{1-x}Se_2$ (x = 0, 0.03) platelet crystals. *Cryst. Res. Technol.* **41**, 1027–1030 (2006).

53. X. Wang *et al.*, Magnetoresistance of two-dimensional and three-dimensional electron gas in $LaAlO_3/SrTiO_3$ heterostructures: Influence of magnetic ordering, interface scattering, and dimensionality. *Phys. Rev. B Condens. Matter Mater. Phys.* **84**, 075312 (2011).

54. K. i. Chahara, T. Ohno, M. Kasai, Y. Kozono, Magnetoresistance in magnetic manganese oxide with intrinsic antiferromagnetic spin structure. *Appl. Phys. Lett.* **63**, 1990–1992 (1993).

55. O. Breunig *et al.*, Gigantic negative magnetoresistance in the bulk of a disordered topological insulator. *Nat. Commun.* **8**, 15545 (2017).

56. X. Hong, S. H. Cheng, C. Herding, J. Zhu, Colossal negative magnetoresistance in dilute fluorinated graphene. *Phys. Rev. B Condens. Matter Mater. Phys.* **83**, 085410 (2011).

57. J. Du *et al.*, Large unsaturated positive and negative magnetoresistance in Weyl semimetal TaP. *Sci. China Phys. Mech. Astron.* **59**, 657406 (2016).

58. H. Yuan *et al.*, Zeeman-type spin splitting controlled by an electric field. *Nat. Phys.* **9**, 563–569 (2013).

59. R. Suzuki *et al.*, Valley-dependent spin polarization in bulk MoS_2 with broken inversion symmetry. *Nat. Nanotechnol.* **9**, 611–617 (2014).

60. R. Bertoni *et al.*, Generation and evolution of spin-, valley-, and layer-polarized excited carriers in inversion-symmetric WSe_2. *Phys. Rev. Lett.* **117**, 277201 (2016).

61. T. Guillet *et al.*, Observation of large unidirectional rashba magnetoresistance in Ge(111). *Phys. Rev. Lett.* **124**, 027201 (2020).

62. A. He *et al.*, Rewritable optical memory based on sign switching of magnetoresistance. *Adv. Electron. Mater.* **6**, 1900701 (2020).

63. B. Kundys *et al.*, Light controlled magnetoresistance and magnetic field controlled photoresistance in CoFe film deposited on $BiFeO_3$. *Appl. Phys. Lett.* **100**, 262411 (2012).

64. G. Kresse, J. Furthmüller, Efficiency of *ab-initio* total energy calculations for metals and semiconductors using a plane-wave basis set. *Comput. Mater. Sci.* **6**, 15–50 (1996).

65. G. Kresse, J. Furthmüller, Efficient iterative schemes for *ab initio* total-energy calculations using a plane-wave basis set. *Phys. Rev. B Condens. Matter* **54**, 11169–11186 (1996).

66. J. P. Perdew, K. Burke, M. Ernzerhof, Generalized gradient approximation made simple. *Phys. Rev. Lett.* **77**, 3865–3868 (1996).

67. J. P. Perdew, A. Zunger, Self-interaction correction to density-functional approximations for many-electron systems. *Phys. Rev. B Condens. Matter* **23**, 5048–5079 (1981).

68. P. E. Blöchl, Projector augmented-wave method. *Phys. Rev. B Condens. Matter* **50**, 17953–17979 (1994).

69. R. Coehoorn *et al.*, Electronic structure of $MoSe_2$, MoS_2, and WSe_2. I. Band-structure calculations and photoelectron spectroscopy. *Phys. Rev. B Condens. Matter* **35**, 6195–6202 (1987).

70. T. Finteis *et al.*, Occupied and unoccupied electronic band structure of WSe_2. *Phys. Rev. B Condens. Matter Mater. Phys.* **55**, 10400 (1997). Erratum in: Phys. Rev. B Condens. Matter Mater. Phys. 59, 2461 (1999).

71. M. Otani, O. Sugino, First-principles calculations of charged surfaces and interfaces: A plane-wave nonrepeated slab approach. *Phys. Rev. B Condens. Matter Mater. Phys.* **73**, 115407 (2006).

72. H. J. Monkhorst, J. D. Pack, Special points for Brillouin-zone integrations. *Phys. Rev. B* **13**, 5188–5192 (1976).